



# Direct observation of anyonic braiding statistics

J. Nakamura<sup>1,2</sup>, S. Liang<sup>1,2</sup>, G. C. Gardner<sup>2,3</sup> and M. J. Manfra<sup>1,2,3,4,5</sup> ✉

**Anyons are quasiparticles that, unlike fermions and bosons, show fractional statistics when two of them are exchanged. Here, we report the experimental observation of anyonic braiding statistics for the  $\nu = 1/3$  fractional quantum Hall state by using an electronic Fabry–Perot interferometer. Strong Aharonov–Bohm interference of the edge mode is punctuated by discrete phase slips that indicate an anyonic phase  $\theta_{\text{anyon}} = 2\pi/3$ . Our results are consistent with a recent theory that describes an interferometer operated in a regime in which device charging energy is small compared to the energy of formation of charged quasiparticles, which indicates that we have observed anyonic braiding.**

Quantum theory requires that all fundamental particles must be either fermions or bosons, and this has profound implications for the statistical behaviour of these particles. However, theoretical works have shown that in two dimensions it is possible for particles to circumvent this principle and obey so-called anyonic statistics, in which the exchange of the position of two particles results in a change of the quantum-mechanical phase that is neither  $\pi$  nor  $2\pi$  (as for fermions or bosons), but a rational fraction of  $\pi$  (refs. <sup>1,2</sup>). Although anyons cannot exist as fundamental particles in nature, certain condensed matter systems are predicted to host exotic quasiparticles that obey anyonic statistics.

The quantum Hall effect is an example of a topological phase of matter that occurs when a two-dimensional electron system (2DES) is cooled to a low temperature and placed in a strong magnetic field. In the quantum Hall regime, the bulk forms an insulator, and charge flows in edge currents that are topologically protected from backscattering and exhibit quantized conductance. The elementary excitations of fractional quantum Hall states<sup>3</sup> are not simply electrons, which obey fermionic statistics, but instead are emergent quasiparticles that are predicted to have highly exotic properties, including fractional charge and anyonic statistics<sup>4</sup>. In two dimensions, two exchanges of particle positions are topologically equivalent to the encircling of one quasiparticle by the other on a closed path<sup>5</sup>, which is referred to as a braid (Fig. 1a). The anyonic character of these quasiparticles is reflected in the fractional phase the system obtains from braiding; therefore, they are said to obey anyonic braiding statistics. The statistics of fractional quantum Hall states has been studied in theoretical<sup>6,7</sup> and numerical<sup>8–10</sup> works. The anyonic phase depends only on the number of quasiparticles encircled and not on the taken trajectory, which makes braiding another manifestation of topology in quantum Hall physics. This topological robustness has motivated the investigation of fault-tolerant quantum computation that uses braiding operations as a basis in various condensed matter systems<sup>5,11,12</sup>. In a recent experiment, anyonic statistics were inferred from noise correlation measurements<sup>13</sup>. However, the direct observation of the anyonic phase in braiding experiments will further our understanding of the exotic behaviour of quantum Hall quasiparticles, and it is a necessary step towards quasiparticle manipulation.

Electronic interferometry has been used to study edge physics in previous theoretical<sup>14–21</sup> and experimental<sup>22–35</sup> works, and it has been proposed as an experimental means to observe anyonic

braiding statistics<sup>15,17,36,37</sup>, including the highly exotic non-Abelian form of anyonic statistics<sup>27,38–44</sup>. An electronic Fabry–Perot interferometer consists of a confined 2DES and uses quantum point contacts (QPCs) to partition edge currents (Fig. 1b). Quasiparticles that are backscattered by the QPCs will braid around quasiparticles that are localized inside the interferometer. Therefore, changes to  $N_{\text{qp}}$ , the number of quasiparticles localized inside the interferometer, will result in a shift in the interference phase owing to the anyonic contribution  $\theta_{\text{anyon}}$  (refs. <sup>15,17,36,37</sup>), with  $\theta_{\text{anyon}} = \frac{2\pi}{2p+1}$  for a Laughlin fractional quantum Hall state  $\nu = \frac{1}{2p+1}$  (refs. <sup>6,7</sup>), where  $p$  is an integer. The interferometer phase difference  $\theta$  is a combination of the Aharonov–Bohm phase scaled by the quasiparticle charge  $e^*$  and the anyonic contribution, written in equation (1) (refs. <sup>15,17,36</sup>):

$$\theta = 2\pi \frac{e^* A_1 B}{e \Phi_0} + N_{\text{qp}} \theta_{\text{anyon}} \quad (1)$$

Here  $e$  is the charge of the electron,  $A_1$  is the area of the interferometer,  $B$  is the applied magnetic field and  $\Phi_0 = h/e$  is the magnetic flux quantum, where  $h$  is Planck's constant. The total current backscattered by the interferometer will depend on  $\cos(\theta)$ , so the interference phase can be probed by the measurement of the conductance  $G$  across the device<sup>15</sup>.

The Coulomb interaction of the interfering edge state with charge located in the bulk of the interferometer has been a chief obstacle to the observation of anyonic phases through interferometry<sup>16</sup>. A strong bulk–edge interaction causes  $A_1$  to vary with changes to the bulk charges<sup>16,17</sup>. Consequently, for so-called Coulomb-dominated devices with a strong bulk–edge interaction,  $\theta_{\text{anyon}}$  is cancelled out by the change in the Aharonov–Bohm phase owing to the change in  $A_1$ , which makes quasiparticle braiding statistics unobservable<sup>17</sup>. Although interesting physics has been explored in Coulomb-dominated devices<sup>24,26,28,35,45</sup>, this bulk–edge interaction must be reduced to make anyonic braiding observable. Various techniques have been implemented to reduce this Coulomb bulk–edge interaction, including the use of metal screening gates<sup>24,28</sup>, the use of low-temperature illumination to enhance the screening effect of the doping layer<sup>41,43,44</sup>, the addition of an Ohmic contact inside the interferometer<sup>31</sup>, and the incorporation of auxiliary screening layers inside the semiconductor heterostructure<sup>46</sup>. The incorporation of epitaxially grown screening layers within the semiconductor heterostructure has enabled the use of small highly coherent

<sup>1</sup>Department of Physics and Astronomy, Purdue University, West Lafayette, IN, USA. <sup>2</sup>Birck Nanotechnology Center, Purdue University, West Lafayette, IN, USA. <sup>3</sup>Microsoft Quantum Purdue, Purdue University, West Lafayette, IN, USA. <sup>4</sup>School of Electrical and Computer Engineering, Purdue University, West Lafayette, IN, USA. <sup>5</sup>School of Materials Engineering, Purdue University, West Lafayette, IN, USA. ✉e-mail: [mmanfra@purdue.edu](mailto:mmanfra@purdue.edu)

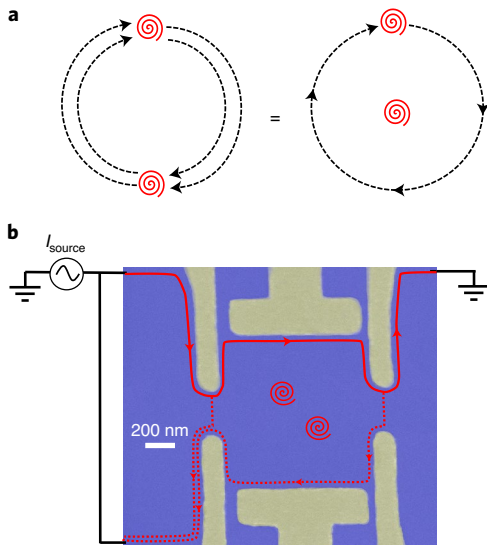


**Fig. 1 | Quasiparticle braiding experiment.** **a**, Schematic representation of quasiparticle exchange. Quasiparticles are represented by red vortices, and trajectories are shown in dashed lines. Two quasiparticle exchanges (left) that bring the particles back to their original position are topologically equivalent to the execution of a closed loop by one quasiparticle around the other (right). In each case, the system gains a quantum-mechanical phase  $\theta_{\text{anyon}}$  owing to the anyonic braiding statistics of the quasiparticles. For the  $\nu = 1/3$  state, a single quasiparticle exchange is expected to result in a change in phase of  $\frac{\pi}{3}$ , and two exchanges (equivalent to a single braid) will result in a phase  $\theta_{\text{anyon}} = \frac{2\pi}{3}$ . **b**, False-colour scanning electron microscope image of the interferometer. Blue regions indicate the GaAs in which the 2DES resides, and metal gates under which the 2DES is depleted are shown in yellow. When operated at the  $\nu = 1/3$  fractional quantum Hall state, the current from  $I_{\text{source}}$  is carried by quasiparticles that travel in chiral edge states (red arrows), and dotted arrows indicate the backscattered quasiparticle paths that may interfere. Quasiparticles (red vortices) may be localized inside the chamber of the interferometer, and the backscattered paths enclose a loop around these quasiparticles, which makes the interferometer sensitive to  $\theta_{\text{anyon}}$ . The lithographic area is  $1.0 \mu\text{m} \times 1.0 \mu\text{m}$ . The device used in the experiments also has a metal gate (not shown) that covers the top of the interferometer. The gate is kept at ground potential and does not affect the 2DES density underneath.

interferometers that exhibit robust Aharonov–Bohm interference, even at fractional quantum Hall states<sup>16</sup>.

**Discrete phase slips.** The experiments in this work use a high-mobility 2DES confined in a GaAs quantum well (the layer stack is shown in Extended Data Fig. 1). Metal surface gates that are negatively biased to deplete the 2DES underneath are used to define the interferometer. Two narrow constrictions define QPCs to backscatter edge currents, and wider side gates define the rest of the interference path. A scanning electron microscope image of the device is shown in Fig. 1b.

We operated the device at a high magnetic field  $B$  at the filling factor  $\nu = 1/3$  quantum Hall state. The conductance variation  $\delta G$ , as measured across the interferometer, versus  $B$  and  $\delta V_g$  (the side gate voltage variation) near the centre of the  $\nu = 1/3$  quantum Hall plateau is shown in Fig. 2. The QPCs remain in the regime of weak backscattering across this region with approximately 90% transmission, and a smooth background conductance is subtracted so that the interference oscillations can be seen clearly. The predominant observed behaviour is that of conductance oscillations with negatively sloped lines of constant phase; however, there are also

a small number of conspicuous discrete phase jumps in the data. The jumps in phase were found to be repeatable in subsequent scans (Extended Data Fig. 2).

Equation (1) provides a straightforward explanation for our observations. A signature of the Aharonov–Bohm effect is a continuous phase evolution with negatively sloped lines of constant phase<sup>17</sup>. The second term in equation (1) predicts a discrete change in phase when  $N_{\text{qp}}$  changes; therefore, it is natural to associate the discrete phase jumps with  $\theta_{\text{anyon}}$ . It is noteworthy that the discrete jumps in phase occur across lines with positive slope in the  $B$ – $\delta V_g$  plane. This can be understood from the fact that an increase in  $B$  is expected to remove quasiparticles from the bulk (or create quasiholes)<sup>41,15</sup>, but an increase of the gate voltage would make it electrostatically favourable to increase the number of localized quasiparticles. Therefore, the magnetic field at which it becomes favourable to remove a quasiparticle should increase when the gate voltage is increased, and a positive slope to the quasiparticle transitions is expected, as is observed in resonant tunnelling experiments<sup>26,32,45</sup>. Given that we do indeed observe a positive slope, it strongly suggests that these discrete phase jumps are associated with changes in  $N_{\text{qp}}$ , and the magnitude of the slope is also consistent with this (see Supplementary information (Discussion 1) for an additional analysis).

Furthermore, a central principle of quantum Hall theory is that quasiparticles are localized in the peaks and troughs of the disorder potential<sup>47</sup>, and that this variation in the electrostatic potential changes the energy cost for the creation of quasiparticles at each location<sup>48,49</sup>. The fact that the discrete phase jumps are irregularly spaced suggests that their positions are in fact determined by disorder, because the strength of the magnetic field at which it becomes energetically favourable for quasiparticles to be created or removed depends on the quasiparticle energy<sup>14</sup>. A rough estimate of the energy broadening owing to the disorder potential from the remote donors can be obtained from the expression  $\Gamma \approx \frac{\sqrt{\pi} \nu e^2}{4 \epsilon d}$  (ref. 49), where  $\epsilon$  is the dielectric constant and  $d = 85 \text{ nm}$  the distance between the donors and the 2DES. For  $\nu = 1/3$ , this yields  $\Gamma \approx 300 \mu\text{eV}$ , although this value may be greatly reduced when the donor potential is screened.

To determine the value of the change in phase that is associated with each phase jump in the data, we performed a least-squares fit to the regions between the phase jumps, which fit the conductance data to the form  $\delta G = \delta G_0 \cos(2\pi \frac{1}{3} \frac{A_1 B}{\Phi_0} + \theta_0)$ , with  $\theta_0$  as the fitting parameter (Fig. 2). This expression for the conductance assumes that between the discrete phase jumps, the phase evolves only with the change in the Aharonov–Bohm phase as  $B$  and  $A_1$  (through the change in  $V_g$ ) vary, and  $\theta_0$  is the excess phase that cannot be attributed to the Aharonov–Bohm effect. We determine the value of the phase jump by computing  $\Delta\theta$ , the difference between the fitted values of  $\theta_0$  in adjacent regions. We take an average and assume that each phase jump corresponds to the removal of a quasiparticle (or, equivalently, the addition of a quasihole) to obtain  $\theta_{\text{anyon}} = 2\pi \times (0.31 \pm 0.04)$ . This is consistent with the theoretical value of  $\theta_{\text{anyon}} = \frac{2\pi}{3}$  for the  $\nu = 1/3$  state<sup>6,7</sup>. Therefore, our experiment confirms the prediction of fractional braiding statistics at the  $\nu = 1/3$  quantum Hall state.

**Transition from constant filling to constant density.** A recent theoretical work by Rosenow and Stern analysed the case of a Fabry–Perot interferometer operated at the  $\nu = 1/3$  state in which strong screening is used to reduce the characteristic Coulomb charging energy and thus suppress the bulk–edge interaction<sup>14</sup>. A key prediction is that the device will transition from a regime of constant filling factor to regimes of constant electron density as the magnetic field is varied away from the centre of the  $\nu = 1/3$  state and the chemical potential moves away from the centre of the gap in

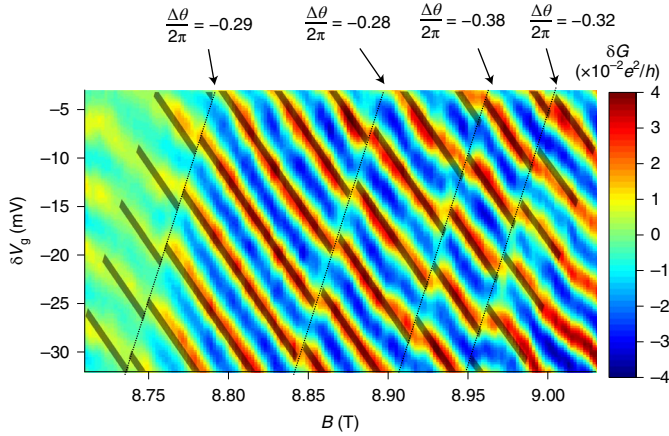


**Fig. 2 | Conductance oscillations versus magnetic field and side gate voltage.** The predominant behaviour is negatively sloped Aharonov–Bohm interference, but a small number of discrete phase jumps are visible (dashed lines are guides to the eye). Least-squares fits of  $\delta G = \delta G_0 \cos(2\pi \frac{A_{\text{AB}}}{\Phi_0} + \theta_0)$  are shown (highlighted black stripes), and the extracted change in phase  $\frac{\Delta\theta}{2\pi}$  is indicated for each discrete jump. An increase of the magnetic field is expected to reduce the number of localized quasiparticles; therefore, the change in phase across each jump is predicted to be  $-\theta_{\text{anyon}}$ .

the density of states. The authors find that, over a wide range of magnetic field strengths, the bulk 2DES stays at a fixed  $\nu = 1/3$  filling. In this regime of constant  $\nu$ , the predominant contributor to the phase will be the Aharonov–Bohm phase, but a small number of well-separated quasiparticle transitions should occur from which  $\theta_{\text{anyon}}$  may be extracted, which is consistent with the results described above. Rosenow and Stern predict that the electrostatic energy cost of the density variation to maintain a fixed  $\nu$  will cause a transition from constant filling factor to constant density as the magnetic field is varied away from the centre. In the regimes of constant density, many quasiparticles (at low magnetic field) or quasiholes (at high magnetic field) will be created inside the interferometer to keep the total charge fixed, with one quasiparticle or quasihole created when the flux is changed by one flux quantum  $\Phi_0$ , which results in substantial changes in the interference behaviour that are mediated by the anyonic phase.

Motivated by these predictions, we operated the interferometer in a wide range of magnetic field strengths across the  $\nu = 1/3$  fractional quantum Hall state. Bulk magnetotransport at  $\nu = 1/3$  with vanishing longitudinal resistance  $R_{xx}$  and a quantized plateau in the Hall resistance  $R_{xy}$  is shown in Fig. 3a, which indicates the range of magnetic field strengths over which the  $\nu = 1/3$  state occurs in our sample. The conductance was measured across the device over the  $\nu = 1/3$  state (Fig. 3b). This is the same measurement as shown in Fig. 2, but extended to higher and lower magnetic field values. As discussed previously, near the centre of the  $\nu = 1/3$  plateau, the predominantly observed behaviour in the conductance is lines of constant phase with negative slope, which is consistent with Aharonov–Bohm interference<sup>15–17,46</sup>, as well as a small number of discrete jumps that can be attributed to quasiparticle transitions. The gate voltage and magnetic field oscillation periods are approximately three times larger than the integer periods measured at  $\nu = 1$ , which is consistent with interference of  $e/3$  fractionally charged quasiparticles, as is expected for the  $\nu = 1/3$  state and consistent with previous experimental observations of fractional charge<sup>28,46,50–52</sup>. The behaviour changes on either side of this central region. The lines of constant phase lose their negative slope. Although there is still a weak magnetic field dependence to the pattern, the magnetic field

scale over which the phase varies is much larger than in the central region, which makes the lines of constant phase nearly flat. The oscillations depend primarily on the side gate voltage only. Despite this change, the lines of constant phase are continuous across the transition from the central Aharonov–Bohm region to the upper and lower regions, which indicates that the oscillations are still due to interference of the edge state.

This observation agrees with the predictions of the Rosenow–Stern model<sup>14</sup>, although we have to consider the effect of thermal smearing to demonstrate this. One prediction is that the  $\Phi_0$  oscillations will be extremely susceptible to thermal smearing<sup>14</sup>. The associated energy scale for thermal smearing is 4 mK for our device, which is much smaller than our estimated electron temperature of  $T \approx 22$  mK. This thermal smearing can be understood from the fact that the regime of constant density corresponds to one in which the chemical potential is located at a position of high density of states. The small energy spacing between the states leads to thermal smearing. Therefore, the absence of  $\Phi_0$  oscillations at  $T \approx 22$  mK is, in fact, in agreement with the theoretical result<sup>14</sup>.

The fact that the lines of constant phase flatten out and become independent of magnetic field strength can be understood on the basis of the combined contribution of the Aharonov–Bohm phase and anyonic phase (equation (1)). A change in the magnetic field to add one flux quantum to the device will change the Aharonov–Bohm phase by  $\frac{2\pi}{3}$ . Additionally, in the low magnetic field (low-field) regime one quasiparticle will be removed, and in the high magnetic field (high-field) regime one quasihole will be added, which results in a phase shift of  $-\frac{2\pi}{3}$ . This leaves the total interference phase unchanged in both regimes. The Aharonov–Bohm phase varies continuously, while (in the limit of zero temperature) the quasiparticle number will change discretely, which leads to the predicted  $\Phi_0$  oscillations<sup>14,15</sup>. However, when the quasiparticle number is thermally smeared, the average number of localized quasiparticles will vary nearly continuously, which leads to a smooth variation of the anyonic phase. In this case, the smoothly varying thermally averaged anyonic phase cancels out the Aharonov–Bohm phase, which leads to no change in  $\theta$  as  $B$  is varied, consistent with our experimental observations.

The approximate range over which the negatively sloped Aharonov–Bohm oscillations occur spans approximately 450 mT (Fig. 3b). To make a quantitative comparison to theory, we computed the predicted width of the fixed  $\nu$  region on the basis of the Rosenow–Stern model<sup>14</sup>,  $\Delta B_{\text{constant } \nu} = \frac{\Delta_{1/3} \Phi_0 C_{\text{SW}}}{\nu e^2 \epsilon}$ . In this expression,  $\Delta_{1/3}$  is the energy gap of the  $\nu = 1/3$  state, and our measured value of  $\sim 5.5$  K (Extended Data Fig. 3) is consistent with previous measurements<sup>53</sup>.  $C_{\text{SW}}$  is the capacitance per unit area of the screening layers to the quantum well, which we calculate as  $C_{\text{SW}} = \frac{2\epsilon}{d}$ . Here, the factor of two accounts for the presence of two screening layers, and  $d = 48$  nm is the distance of the screening layers from the quantum well. Evaluation of the expression for  $\Delta B_{\text{constant } \nu}$  using the experimental values from the device yields  $\Delta B_{\text{constant } \nu} \approx 530$  mT, which is in good agreement with the experimentally observed range of Aharonov–Bohm interference ( $\sim 450$  mT) and suggests that the experimentally observed transition in the interference behaviour indeed can be explained by the Rosenow–Stern model<sup>14</sup>.

Additionally, there is a moderate reduction in the side gate voltage oscillation period in the high- and low-field regions compared to that of the central region. To analyse this period shift, we measured the zero-field Coulomb blockade oscillations and the Aharonov–Bohm oscillations at  $\nu = 1$  to extract the parameters  $\alpha_{\text{bulk}} \approx 0.07$  mV<sup>-1</sup>, which relates the change in bulk charge to  $V_g$ , and  $\alpha_{\text{edge}} \approx 0.12$  mV<sup>-1</sup>, which relates the change in charge at the edge to  $V_g$ . In the central constant filling factor region, only a small number of quasiparticles are created, so the side gates should affect the phase primarily through  $\alpha_{\text{edge}}$ . This leads to a predicted

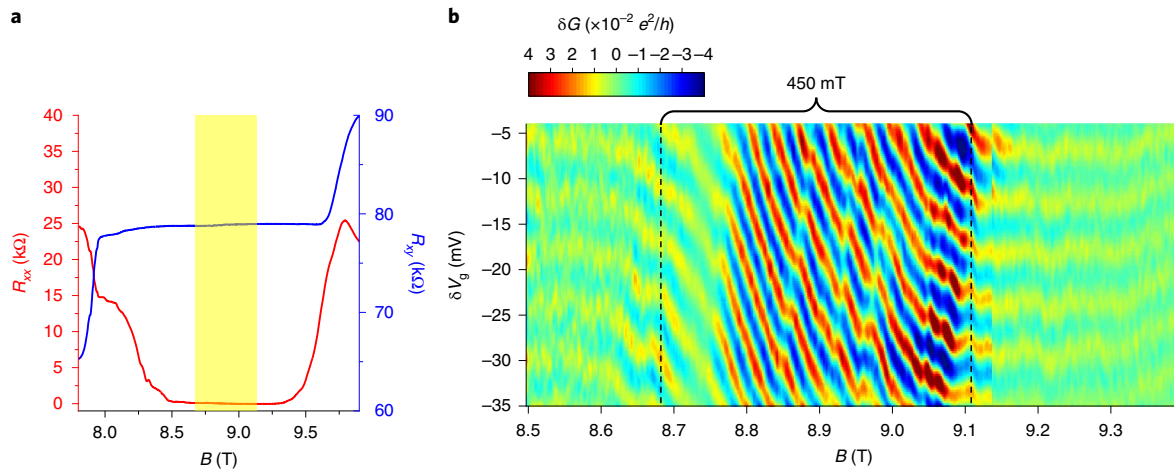


**Fig. 3 | Interference across the  $\nu = 1/3$  quantum Hall plateau.** **a**, Bulk magnetotransport that shows longitudinal resistance  $R_{xx}$  and Hall resistance  $R_{xy}$  across the  $\nu = 1/3$  state. **b**, Conductance oscillations  $\delta G$  versus  $B$  and  $\delta V_g$  (side gate variation relative to  $-0.8V$ ). The dashed lines indicate the approximate range over which the device appears to exhibit conventional Aharonov–Bohm interference with minimal influence of the anyonic phase contribution. The region over which this occurs is near the centre of the plateau and is highlighted in yellow in **a**.

period  $\Delta V_g = \frac{\phi_0}{B} \frac{e}{e^*} \left( \frac{\partial A_L}{\partial V_g} \right)^{-1} \approx 8.4 \text{ mV}$  at  $B = 8.85 \text{ T}$ , in good agreement with the observed period of  $8.5 \text{ mV}$ . However, in the high- and low-field regions, the gate should also change the number of localized quasiparticles through  $\alpha_{\text{bulk}}$ , which leads to lower predicted periods of approximately  $5.5 \text{ mV}$  at  $B = 8.4 \text{ T}$  and  $5.1 \text{ mV}$  at  $B = 9.3 \text{ T}$ , in good agreement with the experimental values of  $5.8 \text{ mV}$  and  $5.4 \text{ mV}$ . The agreement between these predicted and observed periods lends support to the model in which the central region is at constant filling factor and the high- and low-field regions correspond to large populations of quasiholes and quasiparticles<sup>14</sup> (this analysis is described in greater detail in Supplementary information (Discussion 1) and Extended Data Fig. 4). Also, we have performed numerical simulations of interferometer behaviour on the basis of theoretical models<sup>14,17</sup>, which show good qualitative agreement with the experiment (Supplementary information (Discussion 2) and Extended Data Fig. 5).

Therefore, we have a consistent picture in which the statistical phase of anyonic quasiparticles contributes to the interference phase. Our data point to the effect of braiding both in the regime in which the chemical potential is near the centre of the energy gap, where the density of states is small and individual quasiparticle transitions can be resolved, and in the regimes above and below the gap, where the density of states is high and a continuum of quasiparticle and quasihole states contribute to the phase.

The prediction of Rosenow and Stern<sup>14</sup> of a transition from a regime of constant  $\nu$  to regimes of constant density when the magnetic field is varied away from the centre of the state applies also to integer quantum Hall states. Measurements of interference as a function of  $B$  and  $V_g$  across the integer state  $\nu = 1$  are shown in Extended Data Fig. 6. In contrast to the fractional  $\nu = 1/3$  case, the device exhibits no change in behaviour and shows negatively sloped Aharonov–Bohm interference at the high- and low-field extremes of the plateau. This is consistent with the fact that the charge carriers and excited states are electrons that obey fermionic statistics, which makes their braiding unobservable ( $\theta_{\text{fermion}} = 2\pi$ ).

**Temperature dependence.** An additional observation is that the oscillation amplitudes decay with temperature much more sharply in the high-field and low-field regions than in the central region. We measured the amplitude of the oscillations in each region versus temperature. The oscillations decay approximately exponentially as

$T$  increases, and we characterized each region by the temperature decay scale  $T_0$  under the assumption that the oscillation amplitude varies as  $e^{-T/T_0}$  (refs. <sup>15,40,54</sup>). We extracted  $T_0$  through a linear fit of the natural log of the oscillation amplitude as a function of temperature (Fig. 4). For the low-field region at  $8.40 \text{ T}$ ,  $T_0 = 31 \text{ mK}$ , for the central region at  $8.85 \text{ T}$ ,  $T_0 = 94 \text{ mK}$  and for the high-field region at  $9.30 \text{ T}$ ,  $T_0 = 32 \text{ mK}$ . Differential conductance measurements to extract the edge-state velocity were performed<sup>15,25,30</sup>, and they indicate that the edge velocity does not vary substantially between the different regions (see Supplementary information (Discussion 3) and Extended Data Fig. 7). Evidently, the observed suppression of  $T_0$  by nearly a factor of 3 in the high- and low-field regions cannot be explained by a lower edge velocity. On the basis of the measured edge velocities, we calculated predicted temperature decay scales  $T_0$  of  $76 \text{ mK}$  at  $8.40 \text{ T}$ ,  $89 \text{ mK}$  at  $8.85 \text{ T}$  and  $85 \text{ mK}$  at  $9.30 \text{ T}$  (see Supplementary information (Discussion 2)). In the central region, the predicted value of  $T_0$  is close to the experimentally observed value, which indicates that in this region of constant  $\nu$  and a small number of quasiparticles, dephasing can be attributed primarily to thermal smearing of the edge state on the basis of dwell time in the interferometer. However, in the high- and low-field regions, the experimental values are much smaller than the predicted values, which suggests that there must be an additional source of dephasing in these regions. The fact that this increased level of dephasing occurs in the regions in which a large number of quasiparticles and quasiholes populate the interferometer, but not in the central region, may be explained by the topological dephasing that was proposed in ref. <sup>55</sup>, in which thermal fluctuations in  $N_{\text{qp}}$  reduce interference visibility in Fabry–Perot interferometers. This affirms the expectation that the regimes of constant density correspond to a high quasiparticle density of states<sup>14</sup>. This dephasing is an example of the non-local influence of anyonic statistics: despite the fact that the edge quasiparticles are well separated by many magnetic lengths from quasiparticles inside of the bulk of the interferometer such that there is minimal direct interaction, thermal fluctuations in  $N_{\text{qp}}$  lead to the rapid thermal dephasing of the interference signal.

Furthermore, other exotic physics has been observed in the fractional quantum Hall regime that might contribute to enhanced dephasing. Evidence for neutral edge modes has been observed at numerous quantum Hall states, including  $\nu = 1/3$  (refs. <sup>56,57</sup>). It has been shown in a theoretical work that neutral modes may lead to the

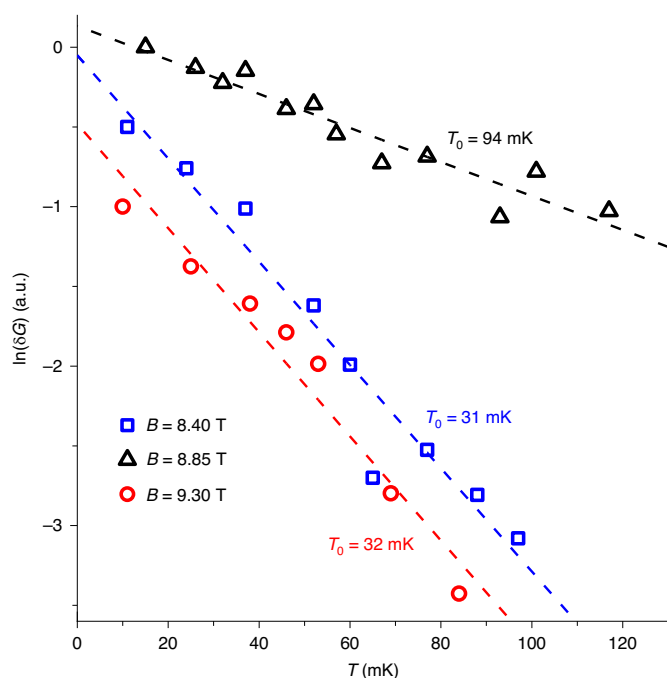


**Fig. 4 | Dependence of oscillation amplitude on temperature.** The natural log of the oscillation amplitude  $\delta G$  at 8.40 T, 8.85 T and 9.30 T versus temperature. Data points are normalized to the amplitude at the lowest temperature and offset for clarity. The oscillation amplitudes show an approximately exponential decay with increasing temperature. Dashed lines indicate linear fits from which the  $T_0$  is extracted at each magnetic field value.  $T_0$  is much larger in the central region than in the low- and high-field regions, which suggests that there is an additional dephasing mechanism in these regions. This may be explained by topological dephasing owing to thermal smearing of  $N_{qp}$ . The QPCs are tuned to approximately 90% transmission at each temperature to maintain constant backscattering.

suppression of interference owing to entanglement with the interfering charge mode<sup>21</sup>, and experimental evidence for this has been reported in the integer quantum Hall regime<sup>34</sup>.

The behaviour of the device described here was reproduced in a second device, including the change in interference behaviour from negatively sloped Aharonov–Bohm interference to flat lines of constant phase, the suppression of  $T_0$  outside the central region, and the observation of discrete phase jumps consistent with the predicted anyonic phase at  $\nu = 1/3$  (Extended Data Fig. 8). The possible influence of residual bulk–edge interaction is discussed in the Supplementary information (Discussion 4).

### Online content

Any methods, additional references, Nature Research reporting summaries, source data, extended data, supplementary information, acknowledgements, peer review information; details of author contributions and competing interests; and statements of data and code availability are available at <https://doi.org/10.1038/s41567-020-1019-1>.

Received: 10 May 2020; Accepted: 29 July 2020;  
Published online: 3 September 2020

### References

- Leinaas, J. M. & Myrheim, J. On the theory of identical particles. *Nuovo Ciment. B* **37**, 1–23 (1977).
- Wilczek, F. Quantum mechanics of fractional-spin particles. *Phys. Rev. Lett.* **49**, 957–959 (1982).
- Tsui, D. C., Stormer, H. L. & Gossard, A. C. Two-dimensional magnetotransport in the extreme quantum limit. *Phys. Rev. Lett.* **48**, 1559–1562 (1982).
- Laughlin, R. B. Anomalous quantum Hall effect: An incompressible quantum fluid with fractionally charged excitation. *Phys. Rev. Lett.* **50**, 1395–1398 (1983).
- Nayak, C., Simon, S. H., Stern, A., Freedman, M. & Das Sarma, S. Non-Abelian anyons and topological quantum computation. *Rev. Mod. Phys.* **80**, 1083–1159 (2008).
- Arovas, D., Schrieffer, J. R. & Wilczek, F. Fractional statistics and the quantum Hall effect. *Phys. Rev. Lett.* **53**, 722–723 (1984).
- Halperin, B. I. Statistics of quasiparticles and the hierarchy of fractional quantized Hall states. *Phys. Rev. Lett.* **52**, 1583–1586 (1984).
- Kjongsberg, H. & Leinaas, J. M. Charge and statistics of quantum Hall quasi-particles – numerical study of mean values and fluctuations. *Nucl. Phys. B* **559**, 705–742 (1999).
- Jeon, G. S., Graham, K. L. & Jain, J. K. Fractional statistics in the fractional quantum Hall effect. *Phys. Rev. Lett.* **91**, 036801 (2003).
- Jain, J. K. *Composite Fermions* (Cambridge Univ. Press, 2007).
- Das Sarma, S., Freedman, M. & Nayak, C. Topologically protected qubits from a possible non-Abelian fractional quantum Hall state. *Phys. Rev. Lett.* **94**, 166802 (2005).
- Stern, A. & Lindner, N. H. Topological quantum computation – from basic concepts to first experiments. *Science* **339**, 1179–1184 (2013).
- Bartolomei, H. et al. Fractional statistics in anyon collisions. *Science* **368**, 173–177 (2020).
- Rosenow, B. & Stern, A. Flux superperiods and periodicity transitions in quantum Hall interferometers. *Phys. Rev. Lett.* **124**, 106805 (2020).
- Chamon, C. de C., Freed, D. E., Kivelson, S. A., Sondhi, S. L. & Wen, X. G. Two point-contact interferometer for quantum Hall systems. *Phys. Rev. B* **55**, 2331–2342 (1997).
- Halperin, B. I. & Rosenow, B. Influence of interactions on flux and back-gate period of quantum Hall interferometers. *Phys. Rev. Lett.* **98**, 106801 (2007).
- Halperin, B. I., Stern, A., Neder, I. & Rosenow, B. Theory of the Fabry–Perot quantum Hall interferometer. *Phys. Rev. B* **83**, 155440 (2011).
- Rosenow, B. & Simon, S. H. Telegraph noise and the Fabry–Perot quantum Hall interferometer. *Phys. Rev. B* **85**, 201302 (2012).
- Levkivskiy, I. P., Frohlich, J. & Sukhorukov, E. B. Theory of fractional quantum Hall interferometers. *Phys. Rev. B* **86**, 245105 (2012).
- von Keyserlingk, C. W., Simon, S. H. & Rosenow, B. Enhanced bulk–edge Coulomb coupling in fractional Fabry–Perot interferometers. *Phys. Rev. Lett.* **115**, 126807 (2015).
- Goldstein, M. & Gefen, Y. Suppression of interference in quantum Hall Mach–Zehnder geometry by upstream neutral modes. *Phys. Rev. Lett.* **117**, 276804 (2016).
- Litvin, L. V., Helzel, A., Tranitz, H. -P., Wegscheider, W. & Strunk, C. Edge–channel interference controlled by Landau level filling. *Phys. Rev. B* **78**, 075303 (2008).
- Deviatov, E. V. & Lorke, A. Experimental realization of a Fabry–Perot type interferometer by copropagating edge states in the quantum Hall regime. *Phys. Rev. B* **77**, 161302 (2008).
- Zhang, Y. et al. Distinct signatures for Coulomb blockade and interference in electronic Fabry–Perot interferometers. *Phys. Rev. B* **79**, 241304 (2009).
- McClure, D. T. et al. Edge-state velocity and coherence in a quantum Hall Fabry–Perot interferometer. *Phys. Rev. Lett.* **103**, 206806 (2009).
- Lin, P. V., Camino, F. E. & Goldman, V. J. Electron interferometry in the quantum Hall regime: Aharonov–Bohm effect of interacting electrons. *Phys. Rev. B* **80**, 125310 (2009).
- An, S., et al., Braiding of Abelian and non-Abelian anyons in the fractional quantum Hall effect. Preprint at <https://arxiv.org/abs/1112.3400> (2011).
- Ofek, N. et al. Role of interactions in an electron Fabry–Perot interferometer operating in the quantum Hall effect regime. *Proc. Natl Acad. Sci. USA* **107**, 5276–5281 (2010).
- Choi, H. K. et al. Robust electron pairing in the integer quantum Hall effect. *Nat. Comm.* **6**, 7435 (2015).
- Gurman, I., Sabo, R., Heiblum, M., Umansky, V. & Mahalu, D. Dephasing of an electronic two-path interferometer. *Phys. Rev. B* **93**, 121412 (2016).
- Sivan, I. et al. Observation of interaction-induced modulations of a quantum Hall liquid’s area. *Nat. Comm.* **7**, 12184 (2016).
- Sabo, R. et al. Edge reconstruction in fractional quantum Hall states. *Nat. Phys.* **13**, 491 (2017).
- Duprez, H. et al. Macroscopic electron quantum coherence in a solid-state circuit. *Phys. Rev. X* **9**, 021030 (2019).
- Bhattacharyya, R., Mitali, B., Heiblum, M., Mahalu, D. & Umansky, V. Melting of interference in the fractional quantum Hall effect: appearance of neutral modes. *Phys. Rev. Lett.* **122**, 246801 (2019).

35. Roosli, M. P. et al. Observation of quantum Hall interferometer phase jumps due to a change in the number of localized bulk quasiparticles. *Phys. Rev. B* **101**, 125302 (2020).
36. Kivelson, S. Semiclassical theory of localized many-anyon states. *Phys. Rev. Lett.* **65**, 3369 (1990).
37. Kim, E. Aharonov–Bohm interference and fractional statistics in a quantum Hall interferometer. *Phys. Rev. Lett.* **97**, 216404 (2006).
38. Stern, A. & Halperin, B. I. Proposed experiments to probe the non-Abelian  $\nu = 5/2$  quantum Hall state. *Phys. Rev. Lett.* **96**, 016802 (2006).
39. Bonderson, P., Kitaev, A. & Shtengel, K. Detecting non-Abelian statistics in the  $\nu = 5/2$  fractional quantum Hall state. *Phys. Rev. Lett.* **96**, 016803 (2006).
40. Bishara, W., Bonderson, P., Nayak, C., Shtengel, K. & Slingerland, J. K. Interferometric signature of non-Abelian anyons. *Phys. Rev. B* **80**, 155303 (2009).
41. Willett, R. L., Pfeiffer, L. N. & West, K. W. Measurement of filling factor  $5/2$  quasiparticle interference with observation of charge  $e/4$  and  $e/2$  period oscillations. *Proc. Natl Acad. Sci. USA* **106**, 8853–8858 (2009).
42. Stern, A., Rosenow, B., Ilan, R. & Halperin, B. I. Interference, Coulomb blockade, and the identification of non-Abelian quantum Hall states. *Phys. Rev. B* **82**, 085321 (2010).
43. Willett, R. L., Nayak, C., Shtengel, K., Pfeiffer, L. N. & West, K. W. Magnetic-field-tuned Aharonov–Bohm oscillations and evidence for non-Abelian anyons at  $\nu = 5/2$ . *Phys. Rev. Lett.* **111**, 186401 (2013).
44. Willett, R.L., et al., Interference measurements of non-Abelian  $e/4$  & Abelian  $e/2$  quasiparticle braiding. Preprint at <https://arxiv.org/abs/1905.10248v1> (2019).
45. McClure, D. T., Chang, W., Marcus, C. M., Pfeiffer, L. N. & West, K. W. Fabry–Perot interferometry with fractional charges. *Phys. Rev. Lett.* **108**, 256804 (2012).
46. Nakamura, J. et al. Aharonov–Bohm interference of fractional quantum Hall edge modes. *Nat. Phys.* **15**, 563–569 (2019).
47. Halperin, B. I. Quantized Hall conductance, current-carrying edge states, and the existence of extended states in a two-dimensional disordered potential. *Phys. Rev. B* **25**, 2185–2190 (1982).
48. Rezayi, E. H. & Haldane, F. D. M. Incompressible states of the fractionally quantized Hall effect in the presence of impurities: a finite-size study. *Phys. Rev. B* **32**, 6924–6927 (1985).
49. MacDonald, A. H., Liu, K. L., Girvin, S. M. & Platzman, P. M. Disorder and the fractional quantum Hall effect: activation energies and the collapse of the gap. *Phys. Rev. B* **33**, 4014–4020 (1986).
50. Goldman, V. J. & Su, B. Resonant tunneling in the quantum Hall regime: measurement of fractional charge. *Science* **267**, 1010–1012 (1995).
51. de-Picciotto, R. et al. Direct observation of a fractional charge. *Nature* **389**, 162–164 (1997).
52. Saminadayar, L., Glattli, D. C., Lin, Y. & Etienne, B. Observation of the  $e/3$  fractionally charged Laughlin quasiparticle. *Phys. Rev. Lett.* **79**, 2526–2529 (1997).
53. Du, R. R., Stormer, H. L., Tsui, D. C., Pfeiffer, L. N. & West, K. W. Experimental evidence for new particles in the fractional quantum Hall effect. *Phys. Rev. Lett.* **70**, 2944–2947 (1993).
54. Hu, Z., Rezayi, E. H., Wan, X. & Yang, K. Edge-mode velocities and thermal coherence of quantum Hall interferometers. *Phys. Rev. B* **80**, 235330 (2009).
55. Park, J., Gefen, Y. & Sim, H. Topological dephasing in the  $\nu = 2/3$  fractional quantum Hall regime. *Phys. Rev. B* **92**, 245437 (2015).
56. Bid, A. et al. Observation of neutral modes in the fractional quantum Hall regime. *Nature* **466**, 585–590 (2010).
57. Inoue, H. et al. Proliferation of neutral modes in fractional quantum Hall states. *Nat. Comm.* **5**, 4067 (2014).

**Publisher's note** Springer Nature remains neutral with regard to jurisdictional claims in published maps and institutional affiliations.

© The Author(s), under exclusive licence to Springer Nature Limited 2020

## Methods

The device used for these experiments has a unique high-mobility GaAs–AlGaAs heterostructure<sup>58,59</sup> with screening layers to minimize the bulk–edge interaction. Additional metal gates on the surface and back side of the chip are used to deplete the screening layers in the vicinity of the Ohmic contacts, which enables transport to be probed in the main quantum well without parallel conduction through the screening layers<sup>46</sup>. The device has a nominal area of  $1.0\ \mu\text{m} \times 1.0\ \mu\text{m}$ , and measurements indicate that the lateral depletion of the 2DES makes the interferometer area smaller by approximately 200 nm on each side, similar to the experimental and numerical results in ref. <sup>46</sup> (see also ref. <sup>60</sup>). Note that the length scale of the interferometer is much greater than the magnetic length  $l_B \equiv \sqrt{\frac{\hbar c}{eB}}$  in the regime investigated, with  $l_B \approx 9\ \text{nm}$  at  $\nu = 1/3$ . Therefore, the condition should hold that the interfering quasiparticles be well separated from the quasiparticles localized inside the interferometer that they may braid around<sup>61</sup>. The device used in this work has a lower electron density  $n$  compared to the device used in ref. <sup>46</sup>, which results in improved device stability because smaller gate voltages can be used. This enables measurements to be performed over a wide range of magnetic field strengths without obscuration of the data by random charge noise. The device also has a smaller area, which may be expected to improve interference visibility and reduce the thermal smearing of quasiparticle transitions, and so discrete jumps in phase owing to anyonic statistics are more likely to be observed<sup>4</sup>.

Experiments were performed in a dilution refrigerator with a base mixing chamber temperature  $T \approx 10\ \text{mK}$ . Coulomb blockade measurements of different quantum dot devices indicate a higher electron temperature  $T \approx 22\ \text{mK}$ . Negative voltages of  $\sim -1\ \text{V}$  were applied to the QPC gates and  $\sim -0.8\ \text{V}$  to the side gates. Conductance was measured as a function of  $\delta V_g$ , which is relative to  $-0.8\ \text{V}$  and applied to both side gates simultaneously. An additional metal gate in the centre of the device (not shown in Fig. 1b for clarity) was held at ground potential, so it did not affect the 2DES density. This gate was intended to make the confining potential from the gates sharper. Also, there was a global backgate underneath the mesa, which was held at ground potential for these experiments.

Standard low-frequency ( $f = 13\ \text{Hz}$ ) 4-terminal and 2-terminal lock-in amplifier techniques were used to probe the diagonal resistance and conductance across the device. Typically, a 50 pA excitation current was used for the measurements. A +600 mV bias was applied to the QPC and side gates while the device was cooled from  $T = 300\ \text{K}$ . This bias-cool technique resulted in an approximately 600 mV built-in bias on these gates, which was found to improve device stability.

The fabrication of the experimental device is outlined in the following steps:

- (1) optical lithography and wet etching were performed to define the mesa;
- (2) Ni/Au/Ge Ohmic contacts were deposited and annealed; (3) the interferometer gates were defined by electron beam lithography and electron beam evaporation (5 nm Ti and 10 nm Au); (4) bondpads and surface gates around the Ohmic contacts were defined by optical lithography and electron beam evaporation (20 nm Ti and 150 nm Au); (5) the GaAs substrate was thinned by mechanical polishing; and (6) the backgates used to deplete the bottom screening well around

the Ohmic contacts were defined by optical lithography and electron beam evaporation (100 nm Ti and 150 nm Au) so that only the primary quantum well was probed.

## Data availability

Source data are available for this paper. All other data that support the plots within this paper and other findings of this study are available from the corresponding author upon reasonable request.

## References

58. Manfra, M. J. Molecular beam epitaxy of ultra-high-quality AlGaAs/GaAs heterostructures: enabling physics in low-dimensional electronic systems. *Annu. Rev. Condens. Matter Phys.* **5**, 347–373 (2014).
59. Gardner, G. C., Fallahi, S., Watson, J. D. & Manfra, M. J. Modified MBE hardware and techniques and role of gallium purity for attainment of two dimensional electron gas mobility  $> 35 \times 10^6\ \text{cm}^2/\text{Vs}$  in AlGaAs/GaAs quantum wells grown by MBE. *J. Cryst. Growth* **441**, 71–77 (2016).
60. Sahasrabudhe, H. et al. Optimization of edge state velocity in the integer quantum Hall regime. *Phys. Rev. B* **97**, 085302 (2018).
61. Jeon, G. S., Graham, K. L. & Jain, J. K. Berry phases for composite fermions: effective magnetic field and fractional statistics. *Phys. Rev. B* **70**, 125316 (2004).

## Acknowledgements

This work is supported by the US Department of Energy, Office of Science and Office of Basic Energy Sciences (award no. DE-SC0020138). G.C.G. acknowledges support from Microsoft Quantum. We thank B. Rosenow for valuable comments on an early version of this manuscript.

## Author contributions

J.N. and M.J.M. designed the heterostructures and experiments. S.L. and G.C.G. conducted the molecular beam epitaxy growth. J.N. fabricated the devices, performed the measurements and analysed the data with input from M.J.M. J.N. and M.J.M. wrote the manuscript with input from all authors.

## Competing interests

The authors declare no competing interests.

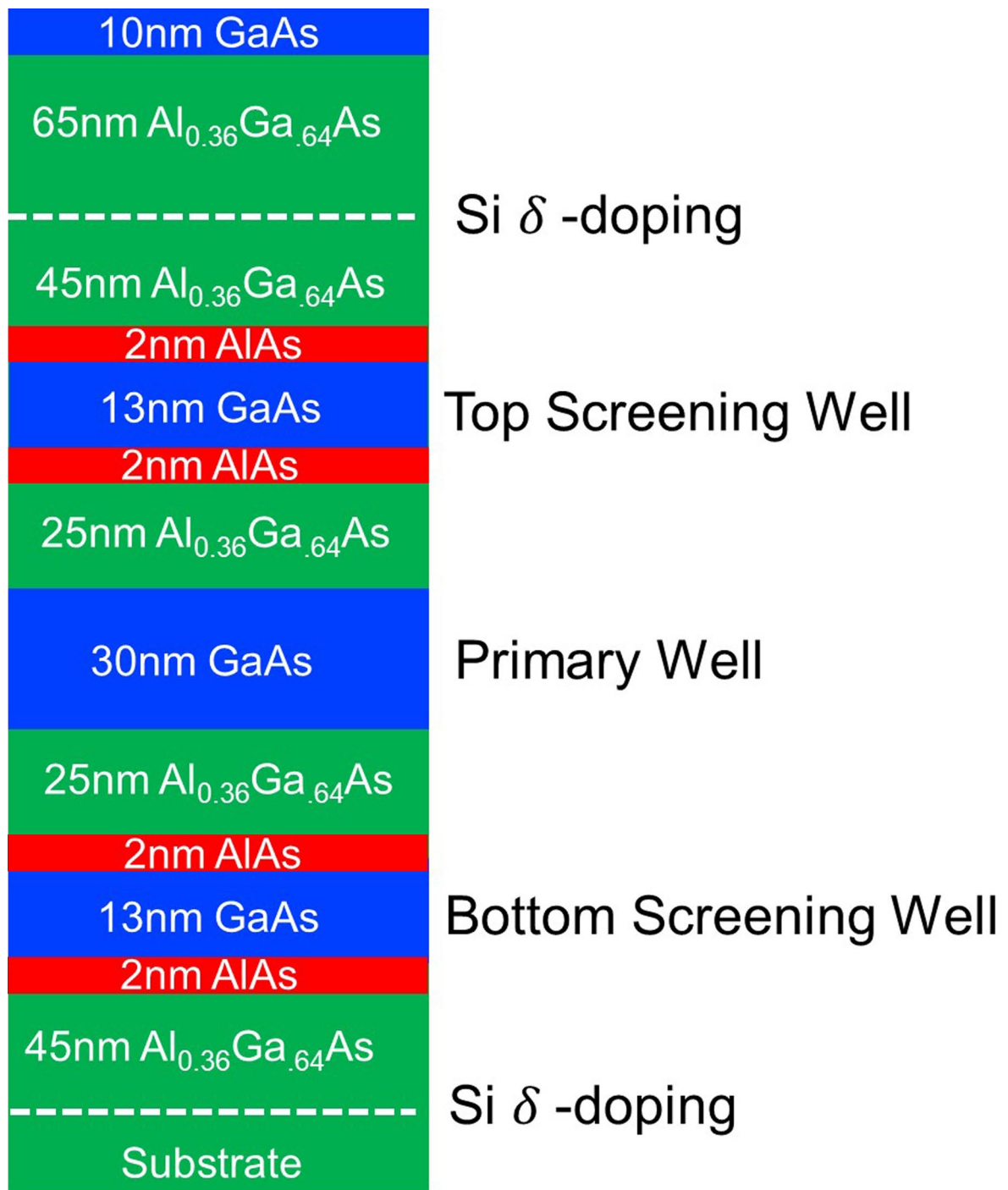
## Additional information

**Extended data** is available for this paper at <https://doi.org/10.1038/s41567-020-1019-1>.

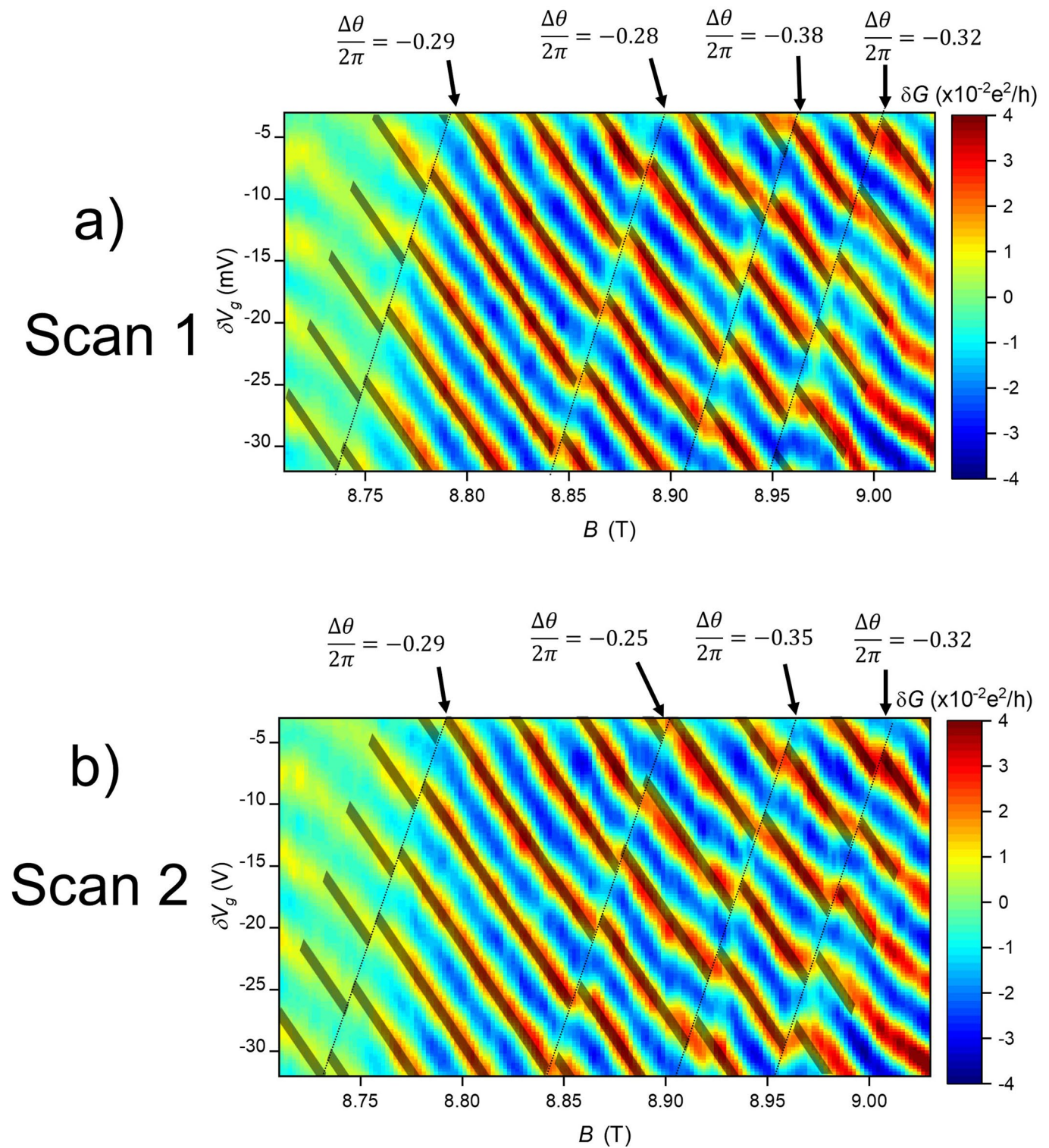
**Supplementary information** is available for this paper at <https://doi.org/10.1038/s41567-020-1019-1>.

**Correspondence and requests for materials** should be addressed to M.J.M.

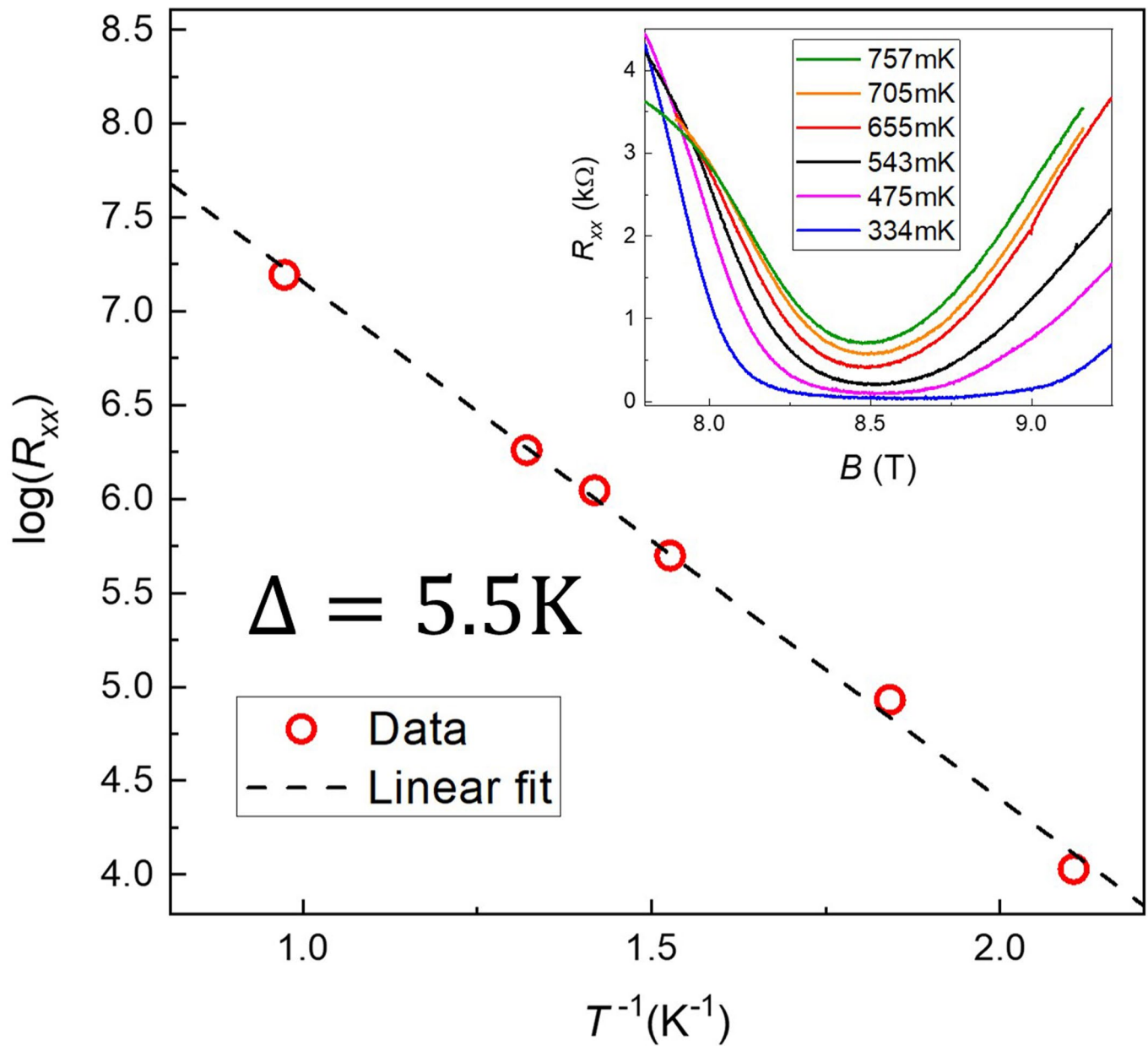
**Reprints and permissions information** is available at [www.nature.com/reprints](http://www.nature.com/reprints).



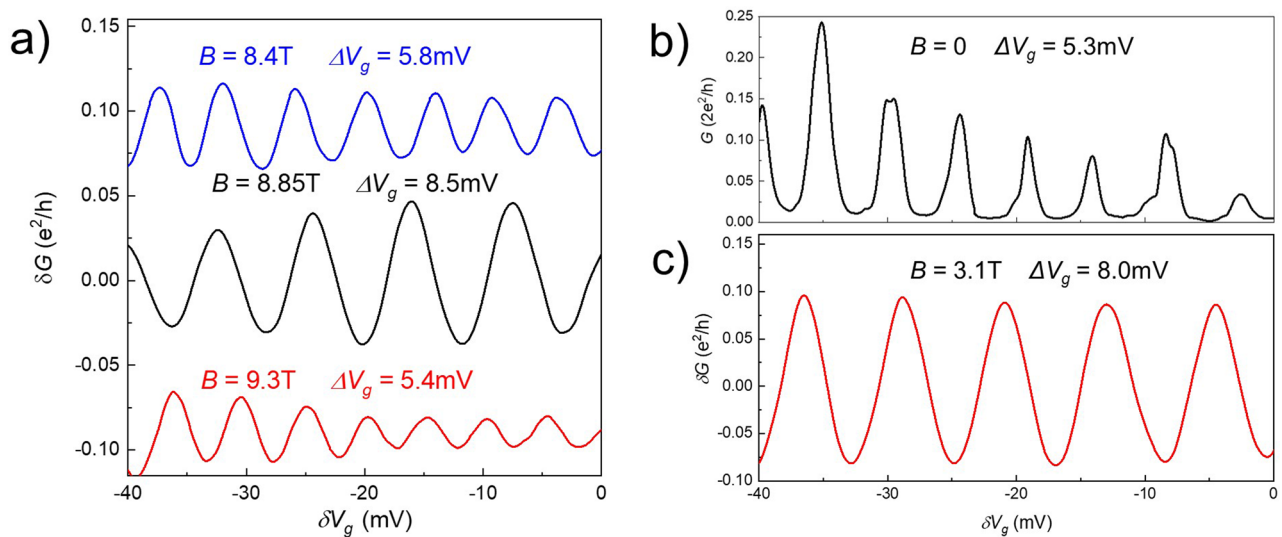
**Extended Data Fig. 1 | Layer stack of the GaAs/AlGaAs heterostructure used for the experiments.** This structure utilizes three GaAs quantum wells: a primary 30nm well flanked by two 13nm screening wells to reduce the bulk-edge interaction in the interferometer. There are 25nm AlGaAs barriers between the main well and screening wells, and the total center-to-center setback of the screening wells from the main well is 48nm.



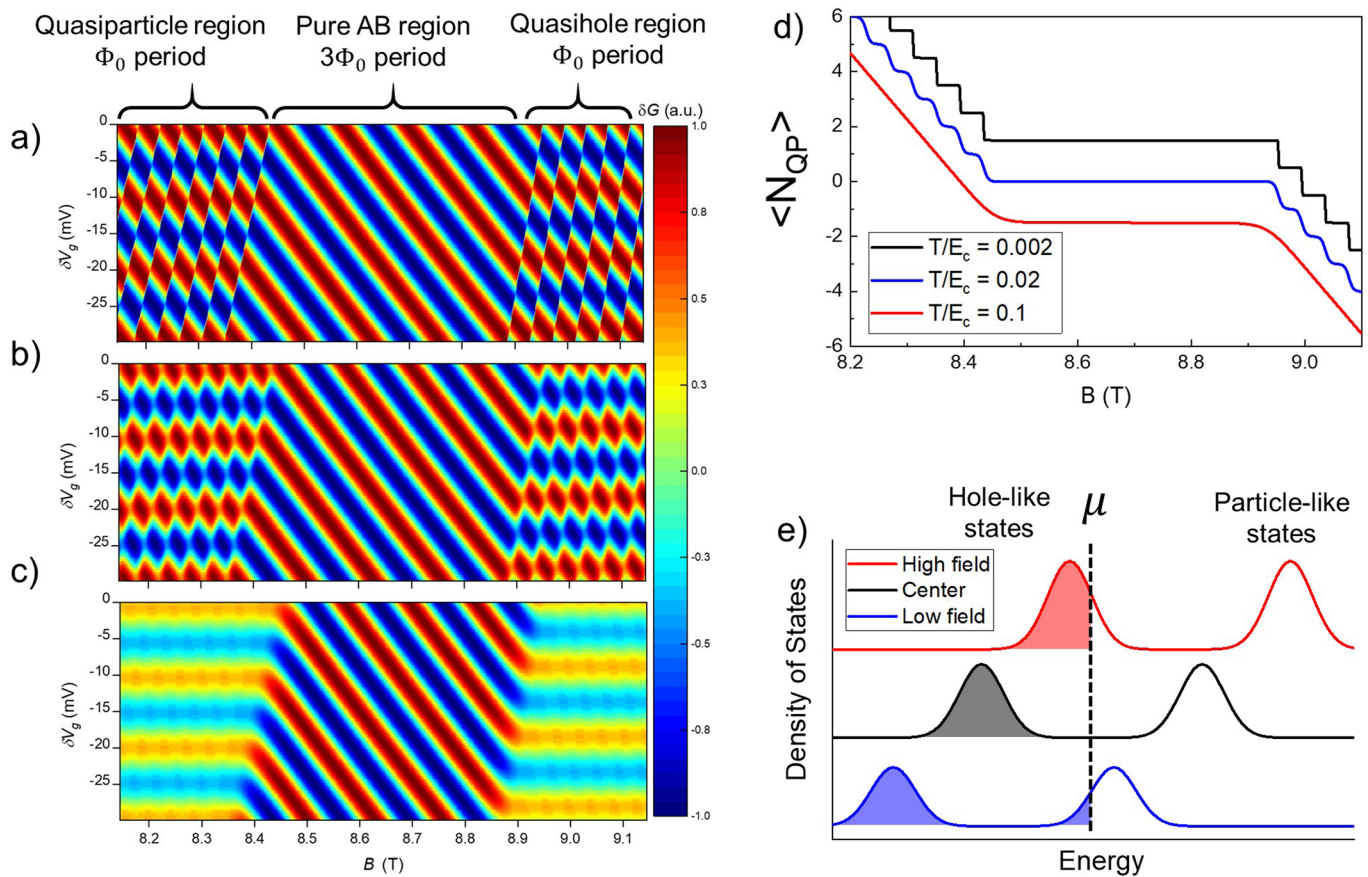
**Extended Data Fig. 2 | Repeatability of discrete phase jumps.** **a**, First scan measurement of conductance versus  $B$  and  $\delta V_g$ . This is the same data in Fig. 2 of the main text. **b**, Second scan across the same range of magnetic field using the same QPC gate voltages. As can be seen from the data, the same pattern of discrete jumps appear in the second scan. The second scan was taken approximately one hour after the first scan. Values of  $\Delta\theta/2\pi$  extracted from least squares fits are shown for both scans, and show similar values for each phase jump in both scans.



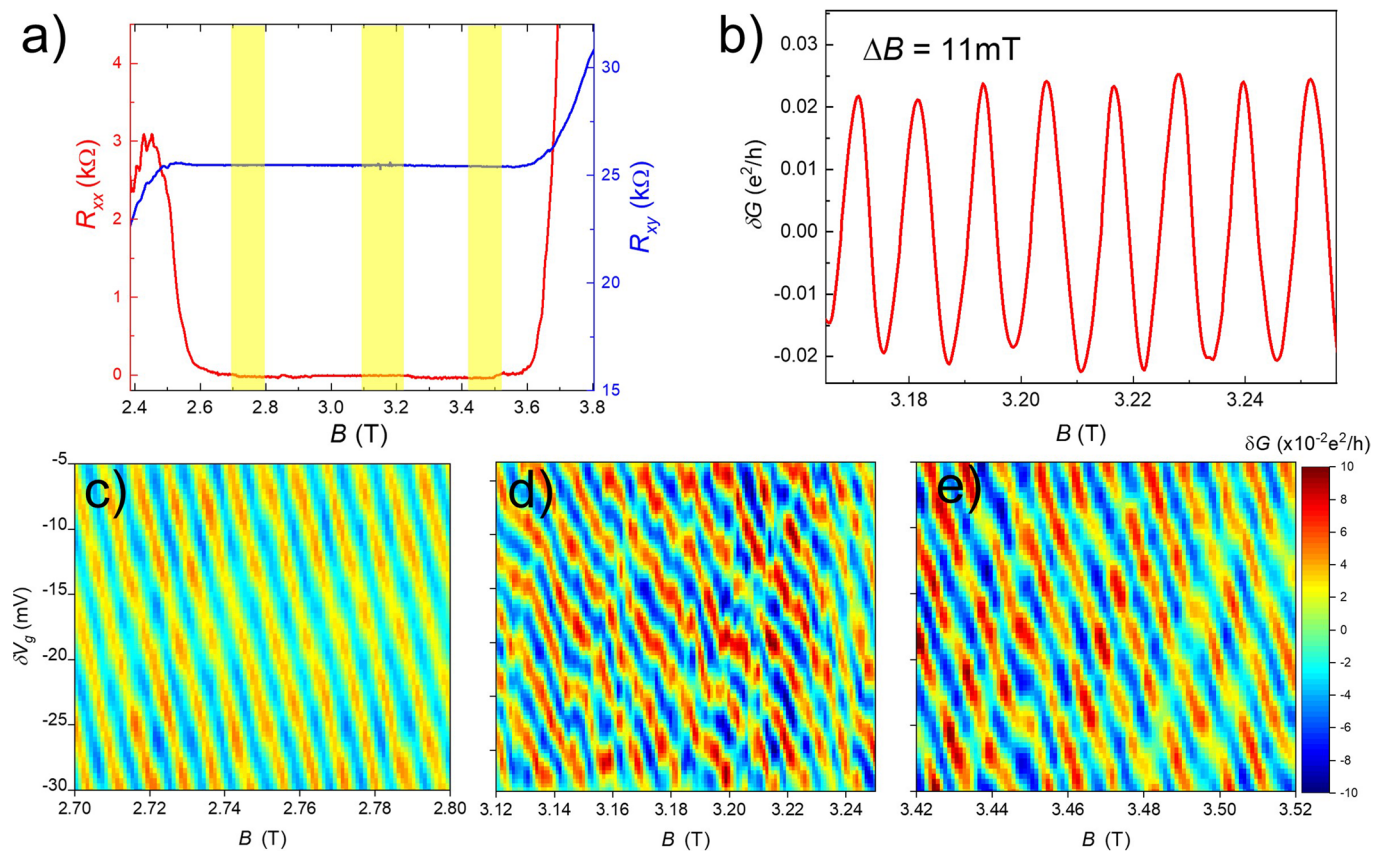
**Extended Data Fig. 3 | Measurement of the energy gap for the  $\nu = 1/3$  fractional quantum Hall state.** The inset shows longitudinal resistance  $R_{xx}$  measured in a bulk region away from the interferometer at different temperatures. A linear fit of the data yields a gap of  $\Delta = 5.5 \text{ K}$ . This is consistent with values measured in previous experiments at similar magnetic field.



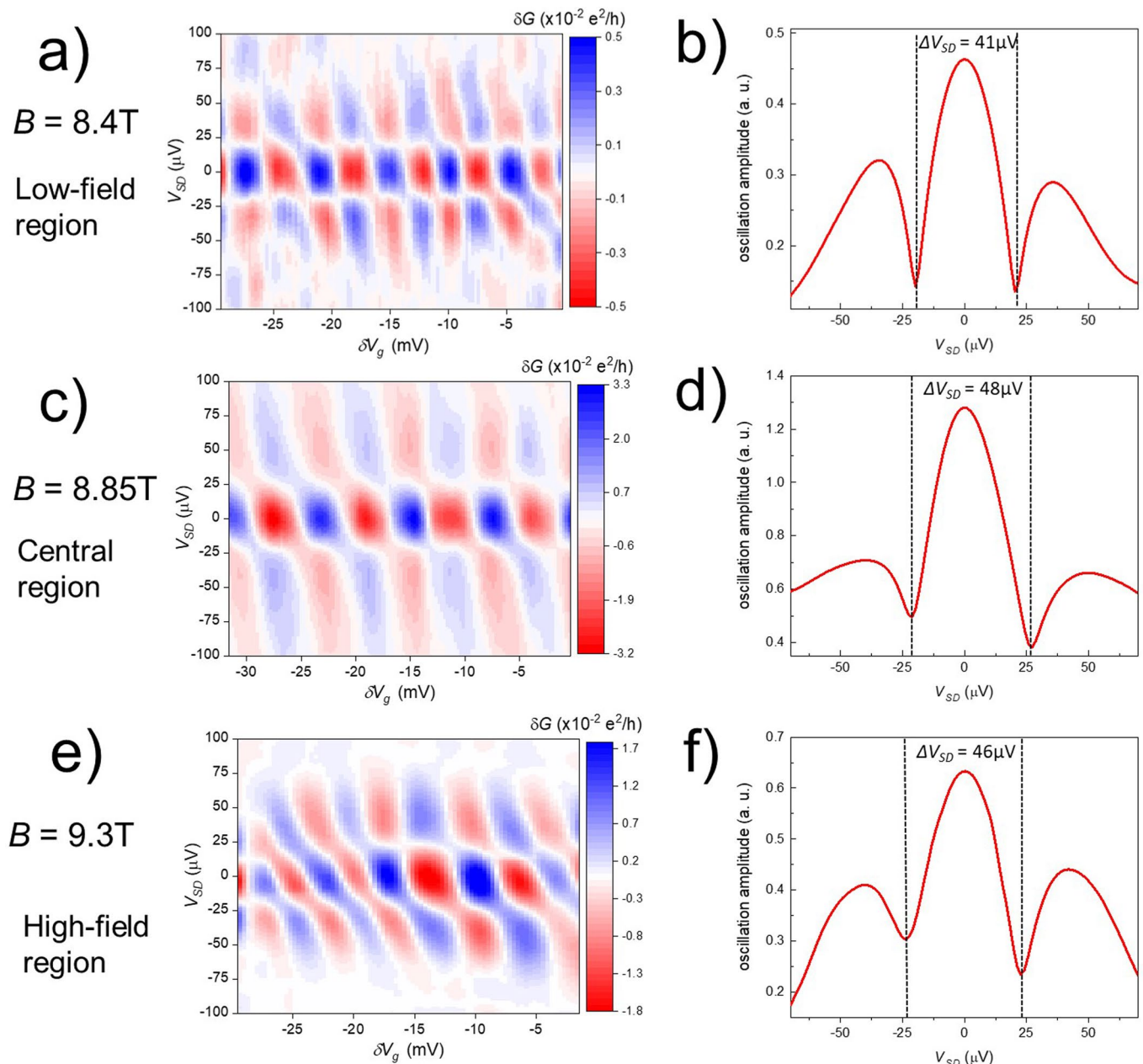
**Extended Data Fig. 4 | Conductance oscillations at different magnetic fields.** **a**, Conductance oscillations  $\delta G$  versus side gate voltage  $\delta V_g$  in the low-field region at  $B = 8.4\text{T}$  (blue), in the central region at  $B = 8.85\text{T}$  (black), and in the high-field region at  $B = 9.3\text{T}$  (red). The side gate oscillation period  $\delta V_g$  is significantly smaller in the low field and high field regions than in the central region, with  $\delta V_g = 5.8\text{mV}$  at  $8.4\text{T}$ ,  $\delta V_g = 8.5\text{mV}$  at  $8.85\text{T}$ , and  $\delta V_g = 5.4\text{mV}$  at  $9.3\text{T}$ . The QPCs are tuned to approximately 90% transmission. **b**, Conductance  $G$  versus side gate voltage at zero magnetic field with the device operated in the Coulomb blockade regime. Unlike other data presented in this work, the oscillations shown here are due to resonant tunneling of electrons rather than interference, and the QPCs are tuned weak tunneling,  $G \ll e^2/h$ . The Coulomb blockade oscillations have a period of  $5.3\text{mV}$ , which is used to obtain the total lever arm  $\alpha_{\text{total}}$  of the gates to the interferometer. **c**, Aharonov-Bohm interference oscillations at  $\nu = 1$ . The oscillations period of  $8.0\text{mV}$  is used to obtain the lever arm  $\alpha_{\text{edge}}$  of the gates to the edge.



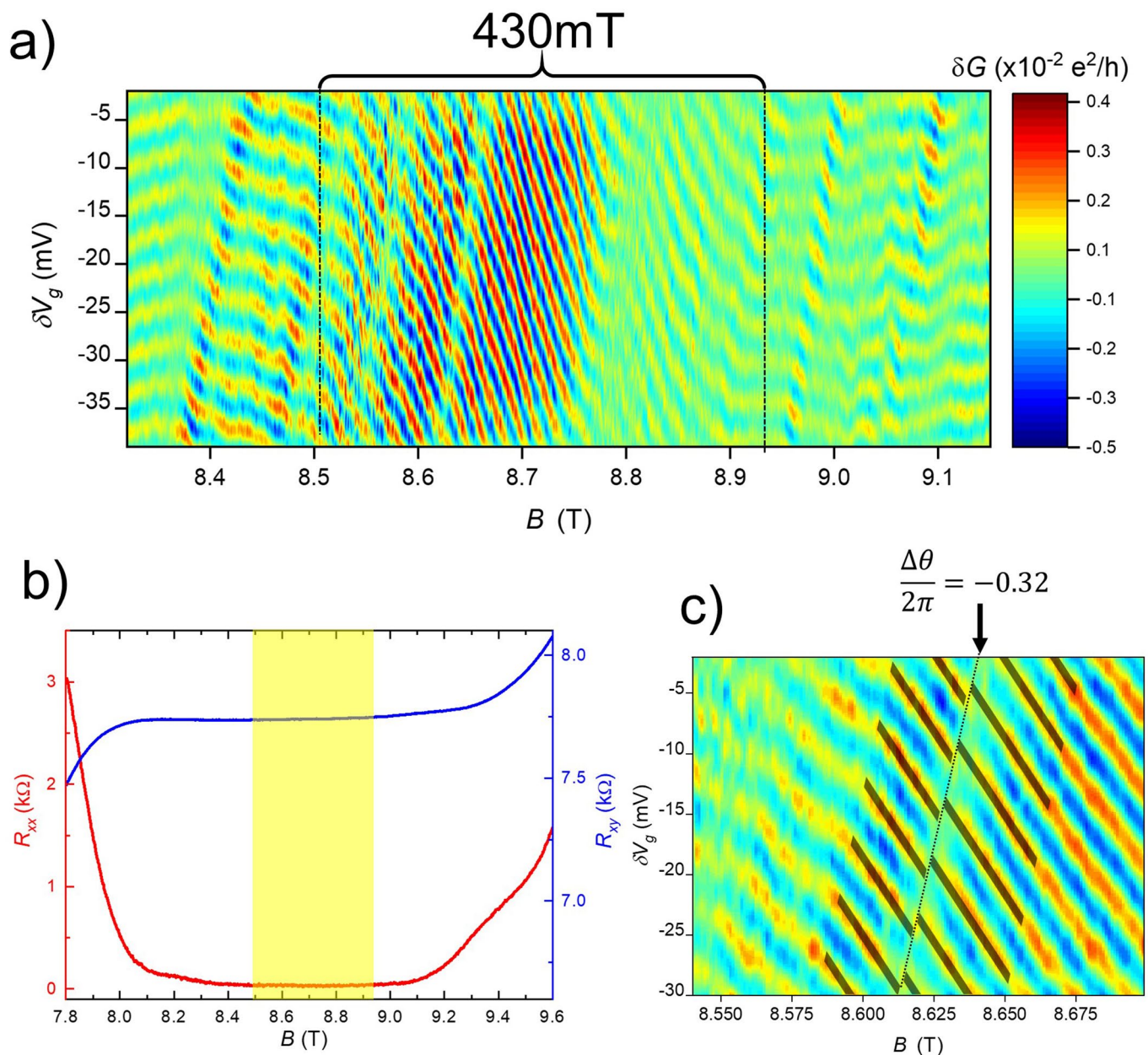
**Extended Data Fig. 5 | Simulations of interferometer behavior at  $\nu = 1/3$ .** Conductance values are computed as a function of magnetic field  $B$  and side gate voltages  $\delta V_g$ , taking into account both the Aharonov-Bohm phase and the contribution  $\theta_{\text{anyon}}$  from braiding around localized quasiparticles inside the bulk of the interferometer. Simulations are performed at different ratios of the temperature  $k_B T$  to the interferometer charging energy  $E_c = e^2/2C$  **a)** 0.002 **b)** 0.02 and **c)** 0.1. **d)** Plot of the thermal expectation value of the number of localized quasiparticles inside the interferometer for different ratios of  $k_B T/E_c$ ; in this context a negative quasiparticle number indicates a population of quasiholes. In each case in the middle of the state there are no quasiparticles, resulting in conventional Aharonov-Bohm interference with  $3\Phi_0$  period, while at higher fields quasiholes form and at lower fields quasiparticles form, resulting in phase slips with  $\Phi_0$  period. As temperature is elevated, the quasiparticle number is thermally smeared, making the  $\Phi_0$  period phase slips unobservable and reducing the amplitude of the oscillations that occur as a function of  $\delta V_g$ . **e)** Qualitative plot of the density of states versus energy.



**Extended Data Fig. 6 | Measurements of interference at  $\nu = 1$ .** **a**, Bulk quantum Hall transport showing the zero in  $R_{xx}$  and plateau in  $R_{xy}$  corresponding to the  $\nu = 1$  integer quantum Hall state. For this integer state, the bulk excitations and edge state current carrying particles are simply electrons, which obey fermionic statistics. **b**, Conductance oscillations versus magnetic field, showing an oscillation period  $\Delta B = 11$  mT. From this period the effective area  $A_i$  of the interferometer can be extracted:  $A_i = \Phi_0 \Delta B$ . In **c**, **d**, and **e** we show conductance versus  $B$  and  $\delta V_g$  across the interferometer in the low field region of the plateau, near the center of the plateau, and on the high-field side of the plateau; the region on the plateau corresponding to each pajama plot is shown in **a**). In each of these regions the device exhibits negatively sloped Aharonov-Bohm oscillations. This contrasts with the data shown in the main text for the  $\nu = 1/3$  state where lines of constant phase flatten out at high and low fields. This is consistent with the fact that electrons, which carry current and form localized states at  $\nu = 1$ , are fermions who obey trivial braiding statistics,  $\theta_{fermion} = 2\pi$ , making braiding unobservable and leading to no change in interference behavior.



**Extended Data Fig. 7 | Differential conductance measurements at  $\nu = 1/3$ .** **a**, Differential conductance  $\partial I/\partial V_{sd}$  as a function of side gate voltage  $\delta V_g$  and source-drain bias  $V_{sd}$  at  $B = 8.4\text{T}$  in the low-field region. **b**, Conductance oscillation amplitude from a Fourier transform of the conductance versus side gate voltage data as a function of  $V_{sd}$ . The oscillation amplitude shows a node pattern as a function of  $V_{sd}$  from which the edge velocity may be extracted, yielding  $v_{\text{edge}} = 8.3 \times 10^3\text{m/s}$ . **c**, Differential conductance and **d**) oscillation amplitude versus  $V_{sd}$  at  $8.85\text{T}$  giving  $v_{\text{edge}} = 9.7 \times 10^3\text{m/s}$ . **e**, Differential conductance and **f**) oscillation amplitude versus  $V_{sd}$  at  $9.3\text{T}$  giving  $v_{\text{edge}} = 9.3 \times 10^3\text{m/s}$ . Evidently, the edge velocity does not change significantly across the  $\nu = 1/3$  quantum Hall plateau.



**Extended Data Fig. 8 | Measurements of interference for a second device, taken from a different chip fabricated on the same wafer.** **a**, Conductance across the interferometer versus magnetic field  $B$  and side gate voltage  $\delta V_g$ ;  $\delta V_g$  is relative to  $-1.0$  V. Behavior is similar to that observed in the device described in the main text: in a finite region with width  $\approx 430$  mT, the device exhibits negatively sloped Aharonov-Bohm oscillations, which flatten out at higher and lower magnetic fields, consistent with the creation of quasiparticles and quasiholes. **b**, Bulk magnetotransport showing  $R_{xx}$  (red) and  $R_{xy}$  (blue) for device  $B$ . The region near the center of the  $\nu = 1/3$  state where the negatively sloped Aharonov-Bohm oscillations occur is highlighted. **c**, zoomed-in view of a clear phase jump in the data (this jump is also visible in **b**), but the data in **c** is a different scan intended to improve signal to noise. Least-squares fits of the conductance on either side of the phase jump yields an extracted phase jump  $\Delta\theta/2\pi = -0.32$ , yielding an anyonic phase  $\theta_{anyon} = 2\pi \times 0.32$ , consistent with theory.